Earth and Planetary Science Letters 406 (2014) 213–222

Contents lists available at ScienceDirect

Earth and Planetary Science Letters

www.elsevier.com/locate/epsl

The effect of deformation history on the evolution of olivine CPO

Yuval Boneh *, Philip Skemer

Department of Earth and Planetary Sciences, Washington University in St. Louis, One-Brookings Drive, Campus Box 1169, Saint Louis, MO 63130, United States

ARTICLE INFO

Article history:
Received 12 June 2014
Received in revised form 5 September 2014
Accepted 14 September 2014
Available online xxxx
Editor: Y. Ricard

Keywords:
olivine
seismic anisotropy
deformation history
crystallographic preferred orientation
texture evolution

ABSTRACT

Olivine crystallographic preferred orientation (CPO) is the primary cause of seismic anisotropy in the upper mantle. In tectonic environments with complex flow patterns, for example corner flow near mid-ocean ridges or subducting slabs, the interpretation of seismic anisotropy may be complicated by evolving thermochemical deformation conditions and the integrated deformation history. To understand how deformation history influences CPO evolution, deformation experiments were conducted on samples of Åheim dunite, which has a strong pre-existing texture. Experiments were performed in a triaxial geometry using a Griggs apparatus at $P = 1$ GPa, $T = 1473$ K, up to a maximum strain of ~ 0.7. To simulate different deformation histories, samples were deformed in three different configurations, with the pre-existing foliation perpendicular, oblique, and parallel to the shortening axis of deformation. Distinct patterns of CPO development are observed for each experimental configuration. Likewise, texture strength, symmetry, and orientation evolved differently in each set of experiments. These data are interpreted as evidence that CPO did not reach steady state and that achieving steady state texture requires larger strains than previously thought. It is concluded that the integrated deformation history plays a significant role in CPO evolution and the consequent interpretation of seismic anisotropy in Earth's mantle.

1. Introduction

Olivine is the most abundant mineral in the upper mantle and its rheology plays an important role in mantle convection and the dynamics of Earth's tectonic plates (Hirth and Kohlstedt, 2003; Karato and Wu, 1993). Over a wide range of deformation conditions, strained crystal lattices align themselves in particular patterns described as crystallographic preferred orientation (CPO). The formation and evolution of CPO in olivine is related to the kinematics of flow (Karato, 1988; Wenk and Christie, 1991), the magnitude of strain (Nicolas et al., 1973; Skemer et al., 2012; Zhang and Karato, 1995), and the thermodynamic conditions of deformation (Couvy et al., 2004; Jung et al., 2006; Katayama and Karato, 2006; Raterron et al., 2007). The CPO generated by olivine deformation is widely considered to be the primary cause for seismic anisotropy in the upper mantle (Karato et al., 2008; Long and Becker, 2010; Mainprice et al., 2000; Nicolas and Christensen, 1987; Savage, 1999), and may also play an important role in the generation of rheological anisotropy (Hansen et al., 2012; Montési, 2013; Skemer et al., 2013; Tommasi et al., 2009).

The most common olivine texture, which is developed by the dominant activity of the [100](010) slip system, aligns the olivine's seismically fastest crystallographic axis [100] with the direction of flow. This A-type texture has been widely observed in both natural samples (Ben Ismaïl and Mainprice, 1998; Nicolas and Christensen, 1987) and laboratory deformation experiments (Zhang and Karato, 1995). The ubiquity of these observations provides a strong basis for the inferring mantle flow patterns from seismic anisotropy (Montagner, 2002; Montagner and Tanimoto, 1991; Savage, 1999; Silver et al., 1999; Tanimoto and Anderson, 1985) and for the parameterization of models that predict seismic anisotropy from numerical simulations of mantle flow (Becker et al., 2003, 2006; Conrad et al., 2007; Faccenda and Capitanio, 2012; Kaminski and Ribe, 2001; Tommasi et al., 2000).

To infer mantle flow from seismic anisotropy, important assumptions must be made about the rate that CPO evolves. Specifically, it is necessary to assume that a steady state texture develops quickly and does not lag significantly behind changes in kinematics (Kaminski et al., 2004). However, recent experimental (Hansen et al., 2014; Skemer et al., 2011), geological (Skemer et al., 2010; Warren et al., 2008; Webber et al., 2010), and numerical studies (Castelnau et al., 2009) have shown that olivine CPO may evolve more slowly than previously thought. Of particular importance may be the influence of pre-existing olivine CPO on subsequent texture evolution (Skemer et al., 2012). In settings of complex

* Corresponding author. Tel.: +1 405 501 7310.
E-mail addresses: boneh@levee.wustl.edu (Y. Boneh), pskemer@wustl.edu (P. Skemer).

http://dx.doi.org/10.1016/j.epsl.2014.09.018
0012-821X/

mantle flow, such as mid-ocean ridges and mantle wedges of subduction zones, the kinematics and the conditions of deformation change rapidly over short length scales (Di Leo et al., 2014; Li et al., 2014). Yet in spite of its importance to the interpretation of seismic anisotropy, the effect of deformation history on subsequent texture evolution is poorly understood.

To explore the influence of deformation history on texture evolution in olivine, we have conducted high pressure/temperature laboratory deformation experiments on dunite with a pre-existing CPO. Experiments were conducted in three different configurations, to simulate three deformation histories. These experiments demonstrate that the accumulation of CPO depends strongly on the initial orientation of the pre-existing CPO, with respect to the geometry of deformation.

2. Methods

2.1. Starting material and experimental procedure

Triaxial deformation experiments were performed using a solid medium Griggs apparatus at a confining pressure of 1 GPa, temperature of 1200 °C, and strain rates of 3.9–5.4 $\times$ 10^{-6} [1/s] (Table 1). The starting material for these experiments is the Åheim dunite, which is composed mainly of olivine (∼95%), with small amount of orthopyroxene (∼2%), chlorite (∼2%), and spinel (∼1%) (Chopra and Paterson, 1981), and has been used in numerous laboratory experiments (Berckhemer et al., 1982; Chopra and Paterson, 1981, 1984; Druiventak et al., 2011; Jackson et al., 1992; Jin et al., 1994; Keefner et al., 2011; Van der Wal et al., 1993; Wendt et al., 1998). The Åheim dunite was chosen specifically for its coarse grain-size (∼0.3 mm) (Fig. 1A) and for its relatively strong initial texture (Fig. 1B).

Samples were obtained from the same block characterized by (Jackson et al., 1992). Cores, extracted using a diamond coring bit, were ground into right cylinders with a diameter of 5.1 mm and with a length of 12.0 mm. Samples were cored in three different orientations with respect to the sample foliation. In the first orientation, the sample's long axis, which is also the axis of shortening and the coring direction, is perpendicular to the foliation plane (Fig. 1C, henceforth this geometry is described to be "perpendicular"). In the second orientation, the sample core is at 45° to the foliation plane (Fig. 1C, "oblique"). In the third orientation, the sample core is parallel to the foliation plane (Fig. 1C, "parallel").

Samples were encased in a nickel capsule with a small amount of NiO powder added at the top of the capsule to buffer oxygen fugacity within the stability field of olivine (Nitsan, 1974). Prior to the experiment, samples were dried in a vacuum oven for a minimum of 24 h at 120 °C to evaporate any adsorbed surface water. For high pressure and temperature experiments in the Griggs apparatus, soft-fired pyrophyllite, porous MgO, and barium carbonate, were used to form the confining pressure medium. This assembly is employed for its stability at high temperatures, allowing us to achieve maximal strains at strain-rates consistent with deformation by the dislocation creep mechanism. However, this pressure medium imposes substantial friction on the sigma-1 piston, limiting the utility of the mechanical data collected by the load cell. For each experiment, the sample was pressurized and heated slowly, over a period of 12 hours, in order to minimize premature deformation of the sample. When the target temperature and pressure was achieved, deformation was initiated at a constant strain-rate. A hit-point was observed in the load–displacement record after a run-in of ∼4 mm. Samples quenched at the hit-point confirm some pre-hit strain ($\varepsilon \sim 0.2$), but with relatively little recrystallization or modification of the microstructure. Experimental conditions and data are summarized in Table 1.

Table 1
Summary of experiments parameters and texture elements. All experiments are under conditions of ∼1 GPa and 1200 °C respectively.

Experiment #	Shortening axis vs. foliation	Natural strain	Strain-rate [1/s]	Θ[a] [°]	M-index	[100] P	[100] G	[100] R	[010] P	[010] G	[010] R	[001] P	[001] G	[001] R
Undeformed	–	0.000	–	0	0.13	0.012	0.517	0.471	0.450	0.160	0.390	0.065	0.384	0.449
WUG 116	Perpendicular	0.217	[b]	0	0.10	0.008	0.300	0.692	0.374	0.103	0.524	0.037	0.459	0.505
WUG 114	Perpendicular	0.328	4.55E−06	0	0.09	0.108	0.256	0.636	0.362	0.032	0.606	0.112	0.271	0.617
WUG 125	Perpendicular	0.406	4.27E−06	0	0.08	0.083	0.228	0.690	0.336	0.065	0.599	0.102	0.293	0.605
WUG 122	Perpendicular	0.507	3.91E−06	0	0.12	0.082	0.380	0.538	0.424	0.049	0.527	0.072	0.346	0.582
WUG 126	Perpendicular	0.653	4.43E−06	0	0.11	0.073	0.449	0.478	0.409	0.087	0.503	0.033	0.333	0.634
WUG 130	Oblique	0.187	[b]	33	0.09	0.033	0.361	0.607	0.368	0.074	0.558	0.061	0.319	0.620
WUG 128	Oblique	0.410	4.08E−06	30	0.08	0.065	0.258	0.677	0.327	0.105	0.567	0.018	0.401	0.581
WUG 129	Oblique	0.482	3.77E−06	18	0.14	0.171	0.297	0.533	0.437	0.084	0.479	0.148	0.306	0.546
WUG 143	Oblique	0.685	5.35E−06	17	0.15	0.211	0.292	0.497	0.450	0.127	0.423	0.149	0.316	0.534
WUG 127	Oblique	0.717	4.78E−06	0	0.15	0.209	0.315	0.476	0.446	0.069	0.486	0.178	0.254	0.568
WUG 138	Parallel	0.207	[b]	80	0.06	0.032	0.156	0.812	0.217	0.227	0.556	0.140	0.220	0.640
WUG 133	Parallel	0.360	4.50E−06	50	0.06	0.107	0.114	0.779	0.141	0.379	0.480	0.207	0.136	0.657
WUG 146	Parallel	0.370	4.45E−06	55	0.06	0.125	0.121	0.754	0.180	0.332	0.488	0.117	0.165	0.718
WUG 134	Parallel	0.415	4.27E−06	25	0.05	0.076	0.126	0.798	0.044	0.486	0.471	0.210	0.063	0.727
WUG 147	Parallel	0.610	4.94E−06	40	0.06	0.142	0.179	0.679	0.061	0.544	0.395	0.139	0.020	0.841

[a] Angle between the normal to the shear plane and the [010] point maxima.
[b] Strain occurred during initial loading of the sample and strain-rate is poorly constrained.

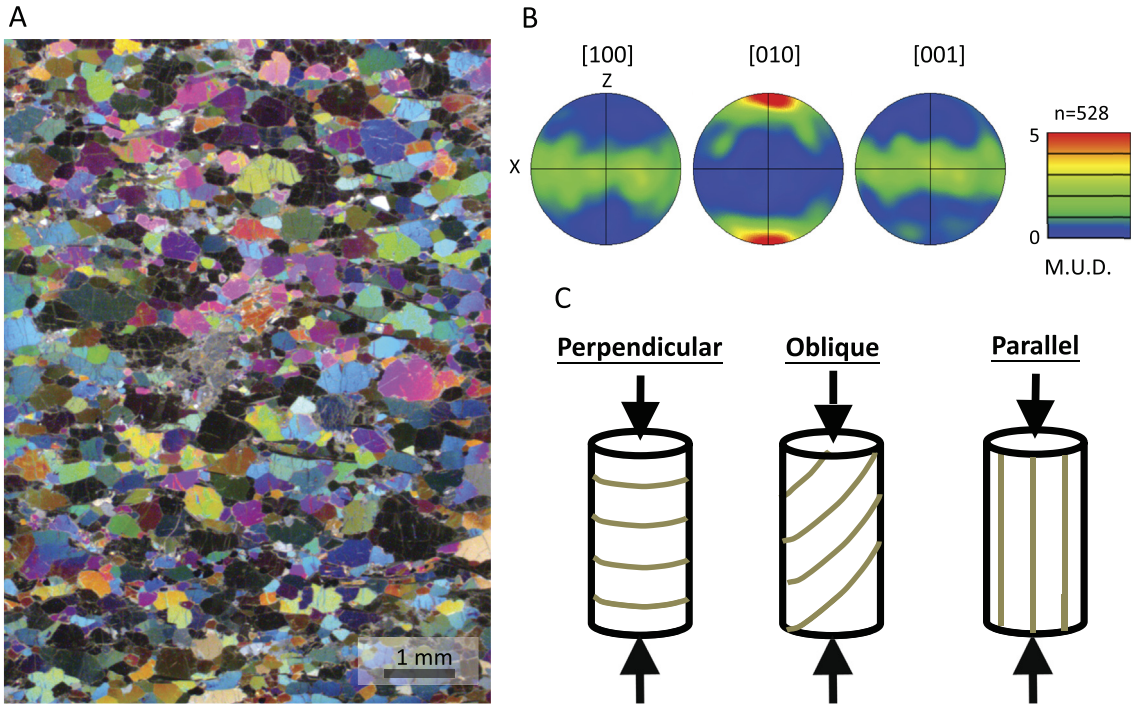

Fig. 1. (A) Microstructure of undeformed Åheim dunite in cross-polarized transmitted light. (B) Pole figures of olivine's pre-existing crystal-preferred orientation (CPO). Olivine exhibits a point maximum of [010] axes, perpendicular to the foliation plane, and well-developed girdles of the [100] and [001] crystal axes parallel to the foliation plane. *n* is the number of unique grains in the dataset. Color contours are multiples of uniform distribution (MUD), which ranges from zero (blue) to five (red). (C) Three experimental configurations described in this study, with the pre-existing foliation (brown lines) perpendicular, oblique, and parallel to the direction of shortening (thick black arrows). (For interpretation of the references to color in this figure legend, the reader is referred to the web version of this article.)

2.2. Microstructural and chemical analysis

Following each experiment, the sample was removed from the pressure medium and a 30 μm thick petrographic thin section was prepared parallel to the axis of compression and perpendicular to the initial foliation. The normal to the thin section plane, for samples in oblique and parallel geometries, is oriented parallel to the strike of the pre-existing foliation. Thin-sections were polished using progressively fine SiC and diamond abrasives. A final chemical–mechanical polish in colloidal silica was used to prepare the thin section for electron microscopy. CPO were measured using a JEOL 7001-FLV SEM system with an Oxford Instruments Electron Backscatter Diffraction (EBSD) detector. The SEM was run in a low vacuum mode to prevent charging of the sample surface. Analyses were performed at an acceleration voltage of 20 keV and a beam current of 18 nA. The stage was tilted at 70° to the electron beam with working distance of 23–25 mm. All samples were analyzed by rastering the beam across the sample in 5 μm steps. The area analyzed by EBSD with a 5 μm step size ranged from 4 to 10 mm^2. An equivalent area in the starting material contains 50–150 unique grains. EBSD mapping produced data sets with 500–3000 unique recrystallized grains. Although these datasets are small for quantitative texture study (Skemer et al., 2005), we are limited by the relatively small ratio of the experimental sample size to the initial grain size. Data were analyzed using the Oxford Instruments Channel 5 software package. Numerical smoothing was used to fill un-indexed points when a minimum of five adjacent pixels was found to have a common orientation. Two additional corrections for the indexed data were performed: (1) We apply a correction for olivine mis-indexing due to olivine pseudo-symmetry (e.g., Fliervoet et al., 1999). (2) Using an underlying band contrast image, large individual grains with a few separated numerical domains of a common orientation were manually interpolated to produce a single grain. Comparisons of smoothed and unmodified data were used to ensure that no artifacts resulted from the smoothing procedure. Individual grains were identified based on continuous domains with consistent orientations. Pole figures were plotted using one data point per grain. In recrystallized materials with narrow grain-size distributions, one point per grain analyses are effectively equivalent to volume weighted analyses. Except at the lowest strains, the experimental samples are almost completely recrystallized, so there is little bias imposed by the one point per grain method. Grains with less than four contiguous pixels of constant orientation points were excluded from the data set in order to avoid skewing results with spurious data.

Several scalar elements of texture are calculated, including strength, symmetry, and orientation, to quantify how different aspects of texture evolve during these experiments. Texture strength was calculated using the *M*-index (Skemer et al., 2005). The *M*-index is scaled such that a random CPO has $M = 0$ and a single crystal has $M = 1$. Texture symmetry was quantified by the three eigenvalues of each pole figure (using the Unicef Careware software, Mainprice, 1990) according to the following relations (Vollmer, 1990):

$$P = \lambda_1 - \lambda_2 \tag{1}$$

$$G = 2(\lambda_2 - \lambda_3) \tag{2}$$

$$R = 3\lambda_3 \tag{3}$$

where P represents the strength of the pole figure's point maxima, G represents the degree to which the pole figure exhibits a girdled texture, and R is the random element of texture. Eigenvalues are ranked such that $\lambda_1 \geq \lambda_2 \geq \lambda_3$ and $\lambda_1 + \lambda_2 + \lambda_3 = P + G + R = 1$. Finally, the orientations of crystal axes with respect to the kinematics of deformation were measured. The orientation of a point maximum in a particular pole figure was determined by the position of the greatest density of points. Error bars were set by the full width of the point maxima at half of the maximum amplitude.

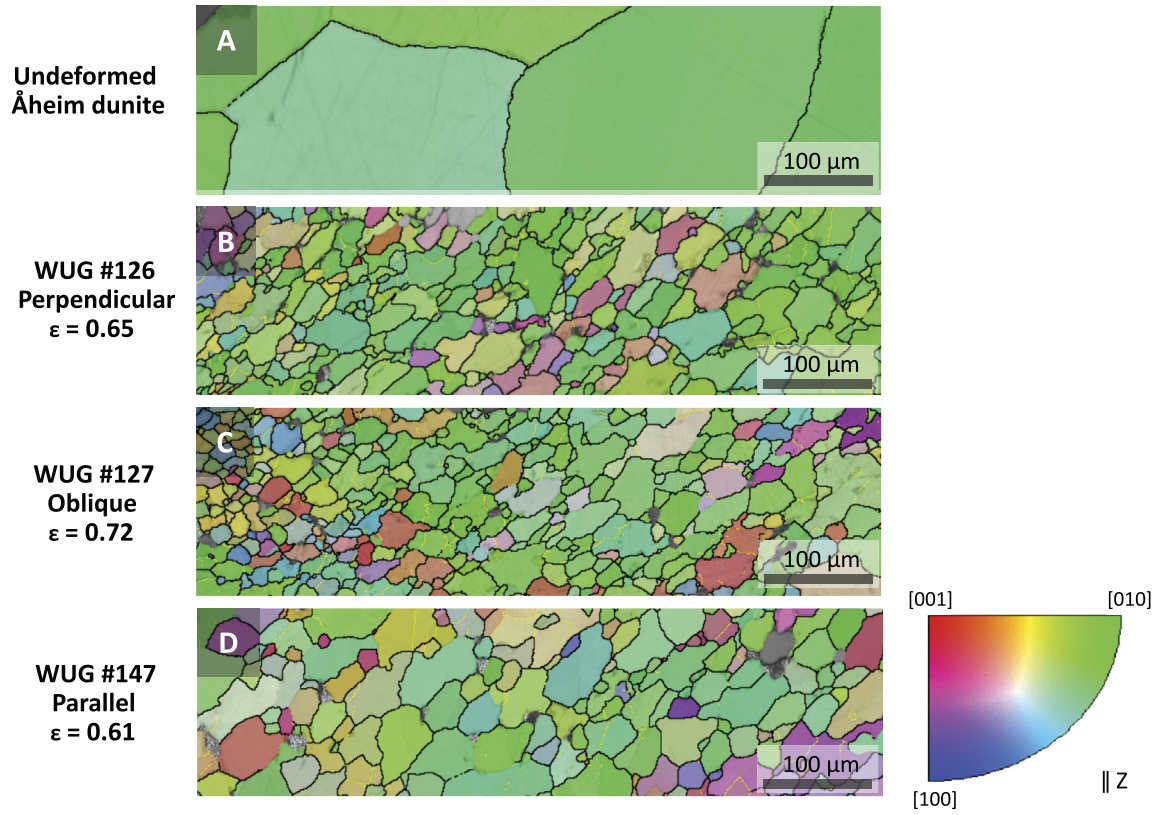

Fig. 2. EBSD maps of (A) undeformed Åheim dunite, and recrystallized grains of samples deformed in (B) perpendicular, (C) oblique, and (D) parallel configurations. Maps are generated with one-micron resolution. Strain is denoted by ε. The undeformed dunite grain-size is about a magnitude of order larger than the recrystallized grain-sizes. Coloration shows the orientation of grains relative to the axis of shortening (Z-direction). The predominant green color reflects the large number of grains that are oriented with [010] parallel to Z. Grain boundaries, shown by black lines, are crystallographic interfaces with a misorientation of >10°. Subgrain boundaries with misorientation of 2–10° are shown as thin yellow lines. (For interpretation of the references to color in this figure legend, the reader is referred to the web version of this article.)

Although experiments were conducted under nominally dry conditions, water content was measured using Fourier transform infrared spectroscopy (FTIR) on double polished thick sections (30–175 μm thick). FTIR was performed using a Digital Excalibur 3000 spectrometer, UMA-600 microscope, and a KBr beam-splitter. Unpolarized IR absorption spectra was recorded for 8–10 arbitrarily oriented crystals for undeformed Åheim dunite and from six deformed samples with a range of strains and experiment durations. Water concentrations were determined using the Paterson (1982) calibration, adjusted by a factor of 3 to agree with the updated calibration of Bell et al. (2003).

3. Results

EBSD maps of undeformed Åheim dunite and recrystallized grains in samples deformed in perpendicular, oblique, and parallel configurations are shown in Fig. 2. Grain-sizes, calculated using the line intercept method with a stereological correction factor of 1.5 (Mendelson, 1969) are 350 ± 70 μm for the undeformed sample and 30 ± 20 μm for the recrystallized grains in deformed samples. Most of the samples deformed to high strains are recrystallized and the grain size appears to reach a steady state that is assumed to be controlled by the stress applied during deformation.

Water concentration measurements confirm that the initial water content in the olivine starting material (4000 ± 2000 ppm H/Si) was reduced to below the detection limit for the FTIR spectrometer (<150 ppm H/Si) in all deformed samples analyzed. These results suggest that any water present in the olivine or produced by dehydration of the chlorite diffused out of the samples during the initial heating and pre-hit annealing stages (8–12 hrs). This is consistent with the diffusion rate of hydrogen in olivine (Mackwell and Kohlstedt, 1990), which at these conditions predicts a time scale for water loss on the order of ∼1–2 hrs. Therefore, the samples were deformed at conditions considered to be effectively dry.

CPO data for 15 experiments in three configurations illustrate the effect of deformation history on the texture evolution. Fig. 3 shows the pole figures for each series of experiments, arranged from the lowest to the highest strains. The first row of the figure shows the initial CPO of the Åheim dunite in each of its configurations. Each series of experiments evolves differently. Samples deformed in the perpendicular configuration (Fig. 3A) develop a [010] point maximum that is parallel to the axis of shortening. An axi-symmetric girdle develops in the [100] and [001] pole figures, which is similar in orientation to the starting material. There is no rotation of the CPO as a function of strain. Samples deformed in the oblique configuration (Fig. 3B) exhibit progressive rotation of [010] point maxima from an initial orientation perpendicular to the foliation towards the axis of shortening (Z). There is also an associated rotation of [100] and [001] girdles towards the radial (X–Y) plane. Within this girdle, a secondary [100] point maximum develops parallel to the initial strike of the foliation, which can be seen in the Y-direction of the pole figure. At the largest strains, the CPO of the samples in the perpendicular and oblique configurations are similar. Samples deformed in the parallel configuration (Fig. 3C) exhibit a dispersed CPO, with the [010] point maximum becoming progressively distributed in a girdle perpendicular to the radial plane and parallel to the shortening axis. Even at the largest strains, samples deformed in the parallel configuration do not approach the same CPO pattern achieved in the perpendicular and oblique configurations.

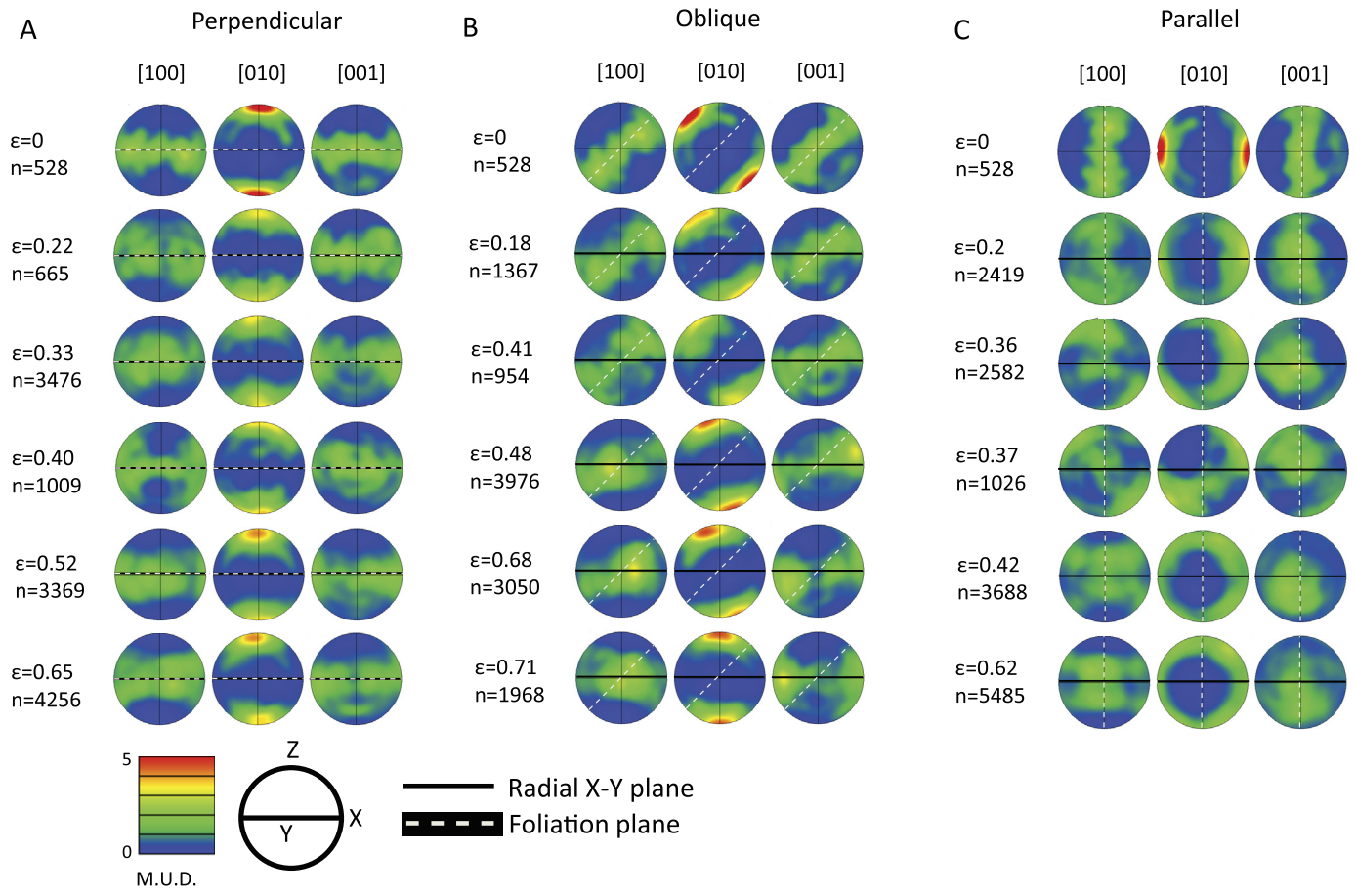

Fig. 3. Upper hemisphere pole figures showing the CPO evolution with strain for perpendicular (A), oblique (B), and parallel experiments (C). The thick horizontal line is the (X–Y) plane. Z is the shortening axis. The dashed line shows schematically the initial orientation of the foliation in the starting material. The first pole figure in each column represents the initial texture, which differs only by its initial orientation relative to the kinematics of deformation. Strain (ε) increases from top to bottom. n is the number of unique grains in the dataset. Color contours are multiples of uniform distribution (MUD).

Fig. 4A shows the evolution of CPO strength as a function of strain for the samples deformed in perpendicular (red circles), oblique (orange triangles), and parallel (yellow squares) configurations. CPO strength does not stabilize at a finite value over the range of strains achieved in the experiments. Moreover, for each of the three sets of experiments the strength of the CPO evolves differently. Samples deformed in the perpendicular configuration undergo an initial decrease, followed by a slight increase in CPO strength. CPO at the largest strain ($M = 0.11$) is marginally lower than the strength of the CPO of the starting material ($M = 0.13$). Samples deformed in the oblique configuration also exhibit an initial drop in CPO strength, which subsequently increases with strain to a maximum value of $M = 0.16$. Samples deformed in the parallel geometry show a weaker texture strength ($M = 0.06$), which is largely unchanged with increasing strain.

Figs. 4B and 4C show the average value of the girdles in the [100] and [001] pole figures

$$G_{avg} = 0.5(G_{[100]} + G_{[001]}) \tag{4}$$

and the evolution of $P_{[010]}$, respectively. For the samples deformed in perpendicular configurations, G_{avg} initially decreases from 0.38 to 0.26 and subsequently increases from 0.26 to 0.39 at higher strains. $P_{[010]}$ increases slightly with strain from 0.35 to 0.43, reflecting the strengthening CPO. For the samples deformed in oblique configurations, G_{avg} decreases slightly with strain from 0.34 to 0.28 while $P_{[010]}$ increases slightly from 0.39 to 0.46. For the samples deformed in parallel configurations, G_{avg} has low initial value of 0.19 that decreases with strain to 0.10. $P_{[010]}$ has low initial value of 0.22, that decreases with strain to 0.05. Fig. 4D shows the evolution of $P_{[100]}$ with strain. Strength of $P_{[100]}$ increases from 0.01 in the undeformed sample to 0.2 in the most deformed sample.

Fig. 3E illustrates the rotation of the [010] axes with progressive strain. Θ is defined as the angle between the densest concentration of [010] axes and the shortening direction (Fig. 3E). For samples deformed in perpendicular configuration, the newly imposed deformation plane is parallel to the pre-existing foliation plane, thus, no rotation is expected or observed. For samples deformed in the oblique configuration, the orientation of the [010] point maximum rotates progressively towards the shortening axis. The rotation initially follows the trajectory of an object passively rotated during coaxial deformation (broken line, Fig. 4E) (Ramsay, 1967). At the highest strain the [010] axes are nearly parallel to the shortening direction, and the sample diverges from the passive rotation trajectory. For samples deformed in parallel configuration, the [010] point maximum disperses with strain, exhibiting a very weak point maximum. Consequently, the estimated uncertainty in Θ is large.

4. Discussion

The CPO of olivine affects many geophysical processes and represents an important cornerstone of our interpretation of deformation within Earth's mantle. Due to olivine's intrinsic rheological anisotropy, there is a strong relationship between the strength of the deformation induced CPO and the instantaneous shear strength

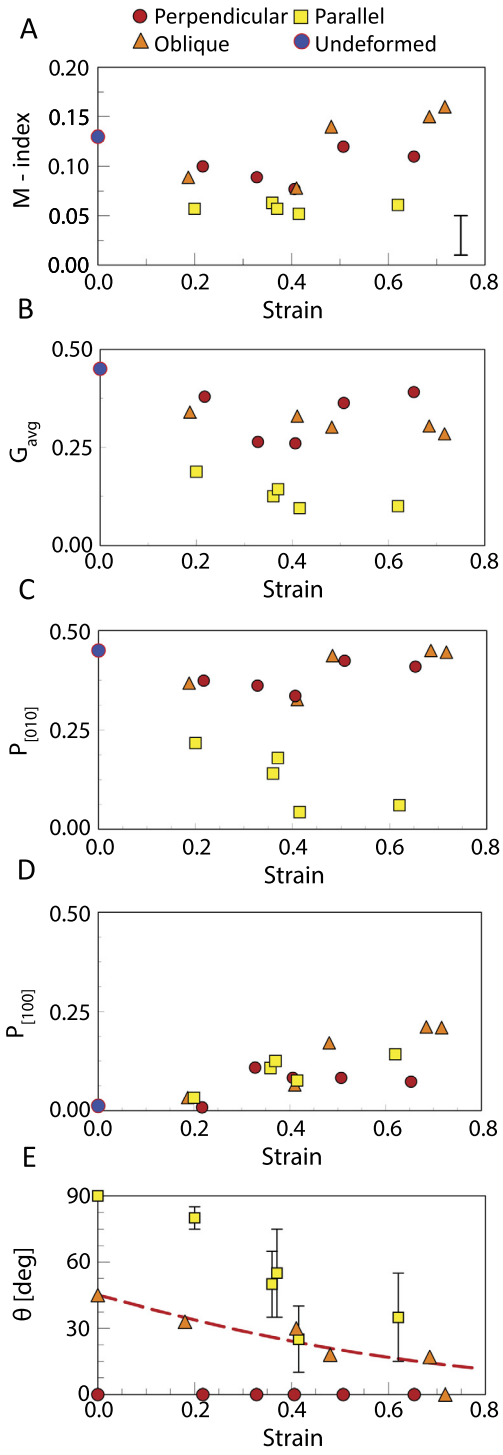

Fig. 4. Three elements of sample texture: strength (A), symmetry (B–D), and orientation (E), as a function of strain. Samples deformed in perpendicular, oblique, and parallel configurations are shown by red circles, orange triangles and yellow squares, respectively. The blue circle shows the texture of undeformed Åheim dunite. Data shown are based on one point-per grain analyses, to highlight the texture evolution of the recrystallized grains. (A) Texture strength quantified using the M-index technique (Skemer et al., 2005). A representative error bar (± 0.02) is shown in the lower right. The strength increases in the samples deformed with perpendicular and oblique geometries. The strength of samples deformed in parallel geometry decreases with strain. (B–D) Texture symmetry described by an average of $G_{[100]}$ and $G_{[001]}$ (B), $P_{[010]}$, (C), and $P_{[100]}$ (D) (G – girdle, P – point, see text for details). (E) Texture rotation is described by the angle Θ, which is the angle between [010] and the shortening axis. The broken red line shows the orientation of a passively rotating 45° plane in pure shear (Ramsay, 1967, p. 67). (For interpretation of the references to color in this figure legend, the reader is referred to the web version of this article.)

of an olivine aggregate (Hansen et al., 2012; Tommasi et al., 2009). Therefore, it is clear that steady-state CPO is required to attain steady-state rheology. Similarly, interpreting seismic anisotropy in terms of mantle flow requires knowledge of whether or not CPO been aligned with the instantaneous deformation field. Hence, it is important to assess the rate at which olivine CPO evolves, and the conditions under which olivine CPO achieves steady state.

4.1. CPO development in samples with initially weak textures

Previous experimental studies have explored the initial formation and evolution of CPO in both pure shear (Nicolas et al., 1973) and simple shear (Bystricky et al., 2000; Hansen et al., 2014; Zhang and Karato, 1995) on materials with initially weak CPO. Nicolas et al. (1973) provide the first systematic data on CPO development in olivine, through a series of triaxial deformation experiments that generated an axi-symmetric CPO. Zhang and Karato (1995) followed with the first experiments in a simple shear geometry, which generated the expected orthorhombic CPOs often observed in nature (e.g. Ben Ismaïl and Mainprice, 1998; Nicolas and Christensen, 1987). Subsequent experiments in torsion (Bystricky et al., 2000) provided additional data at shear strains of up to $\gamma = 5$. Zhang and Karato (1995) show that olivine [100] axes rotate towards the shear direction at relatively small strains ($\gamma = 1$) and are generally assumed to be stable at that point (Bystricky et al., 2000). These observations support the paradigm, widely used in interpreting seismic anisotropy, that olivine CPO evolves relatively quickly, and reaches a stable configuration at low strains (e.g. Skemer et al., 2012). However, in each of these sets of experiments, fabric strength continues to increase with progressive strain, indicating that true steady state was not achieved. Hansen et al. (2014), building on these experiments, performed torsion tests on olivine up to strains of $\gamma = 20$. These authors interpret their results to show that other elements of texture, including the strength and symmetry of the CPO, continue to evolve up to shear strains of $\gamma = 10$, and suggest that larger strains may be required to reach steady state.

4.2. CPO development in samples with initially strong textures

Most experimental studies on the evolution of olivine CPO have focused on synthetic starting materials with initially weak or random CPO. However, laboratory experiments (Skemer et al., 2011; Wendt et al., 1998) and geologic studies of shear zone evolution (Michibayashi and Mainprice, 2004; Skemer et al., 2010; Warren et al., 2008; Webber et al., 2010) have demonstrated that pre-existing texture may alter the rate at which CPO evolves.

In this study, olivine with a pre-existing CPO is deformed in an axially symmetric geometry, under conditions that favor the activity of the [100](010) slip system. Three different sample orientations are used to simulate three different deformation histories. At these deformation conditions the CPO that is expected to form is axi-symmetric, with a [010] point maximum parallel to the shortening axis (towards the Z axis) and [100] and [001] girdles in the radial plane (i.e., X–Y plane) (Karato et al., 2008; Nicolas et al., 1973). To determine whether steady state CPO is achieved in our experiments we analyze a number of metrics that quantify the strength, symmetry, and orientation of texture. Our assertion is that for texture to reach steady state, three things are required: (1) The strength of the CPO must approach a steady state value. (2) The symmetry elements (point, girdle, and random) for all pole figures must approach steady values. (3) The alignment of the CPO with respect to the deformation geometry must cease to rotate with progressive strain. Microstructural observation and texture quantification reveal that the microstructure

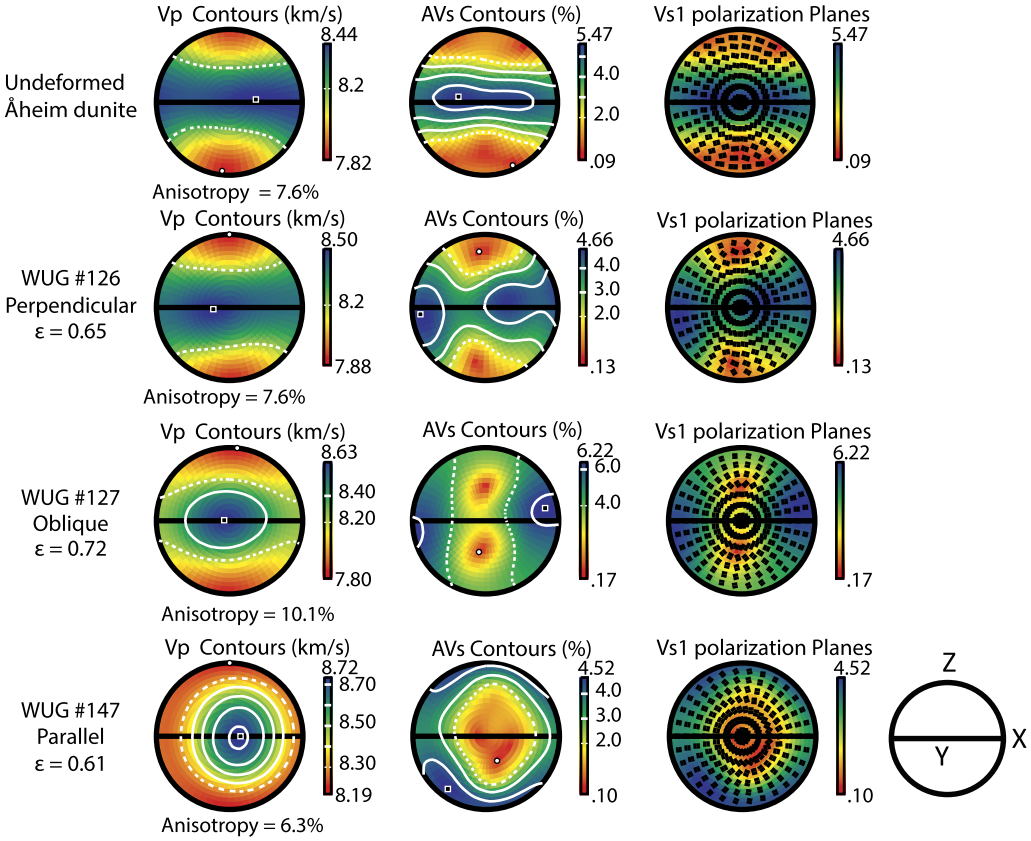

Fig. 5. Upper hemisphere pole figures (same orientation as Fig. 3) showing seismic anisotropy calculated by weighted area for the undeformed sample, and highly deformed samples with perpendicular, oblique and parallel configurations using elastic constants from (Abramson et al., 1997). The left column shows the P-wave velocity (*Vp*) in units of [km/s]. The middle column shows the percent difference between the fast and slow S-wave velocities ($AVs = 200\ (V_{max}-V_{min})/(V_{max}+V_{min})$). The direction of maximum/minimum velocities is denoted by black box and white circle respectively. The right column shows the orientation of the fastest S-wave (*Vs*1) with respect to deformation plane. Colors in the right column are contours of *AVs*, identical to the middle column of pole figures. The undeformed and perpendicular configuration samples exhibit anisotropy similar to an A-type fabric, while the oblique and parallel configuration samples are more similar to a B-type fabric (Mainprice, 2007).

did not reach a steady state for any of the three samples configurations. Pole figures (Fig. 3) illustrate the differences in CPO development between samples deformed in the three different geometries. Samples deformed in the perpendicular geometry show a relatively well-developed texture, which we interpret to be due to the similarity between the initial texture and the predicted steady-state texture. Samples deformed in the oblique geometry appear to show a texture that is similar to the predicted steady state texture, but also exhibit a pronounced orthorhombic symmetry at high strain. Samples deformed in parallel geometry do not exhibit a texture that resembles the predicted CPO, even at the highest strains. Considered together, all three deformation geometries show features of transient CPO evolution, but do not converge towards a steady-state texture.

4.3. Development of an apparent B-type fabric

The highest strain samples from the oblique and parallel configurations exhibit a quasi-orthorhombic CPO with point maxima, rather than the predicted girdles, in the radial plane. This is particularly evident in experiments with oblique configurations, in which the initial foliation is 45° from the axis of compression. In these pole figures (Fig. 3B) there is a clear [100] point maximum parallel to *Y* (the direction in the radial plane that is parallel to the initial strike of the foliation), and a complementary [001] point maximum parallel to *X* (the direction in the radial plane perpendicular to the initial strike of the foliation). $P_{[100]}$ is also observed to increase with progressive strain (Fig. 4D). The symmetry of this CPO is unexpected. Theoretical treatments of CPO evolution predict that deformation with axisymmetric kinematics should generate a texture that is also axially symmetric (Ribe and Yu, 1991; Wenk et al., 1991). Triaxial deformation experiments confirm this prediction (e.g. Nicolas et al., 1973). Lower symmetry is expected when there is a significant component of simple shear (Wenk and Tomé, 1999), however there is no shape change that would indicate this occurred in our experiments.

The orientation of [100] axes could lead to the interpretation that the CPO generated in these experiments is “B-type” (Jung and Karato, 2001), which has been widely cited as a plausible explanation for trench-parallel shear wave splitting (e.g. Long and Silver, 2009). Strictly, the B-type CPO is generated by the predominant activity of the [001](010) slip system. However at these deformation conditions, the [100](010) and associated A-type CPO are favored.

We interpret the CPO of samples deformed in oblique and parallel geometries as an ‘apparent B-type’ fabric that is a consequence of the pre-existing texture. In oblique and parallel configurations, some fraction of the grains in the starting material have [100] axes that are located initially in the radial plane. By definition, these [100] axes are parallel to the strike of the initial foliation, and therefore parallel to the *Y*-axis of our deformation geometry. This subset of grains is already at or near its steady state orientation and although their Schmidt factor is low these grains do not require significant rotational deformation to reach the radial plane. Other grains, whose [100] axes are initially distributed elsewhere in the girdle and therefore not located in the radial plane, require larger strains to adopt the predicted steady-state CPO. Hence, we conclude that this apparent B-type CPO is not

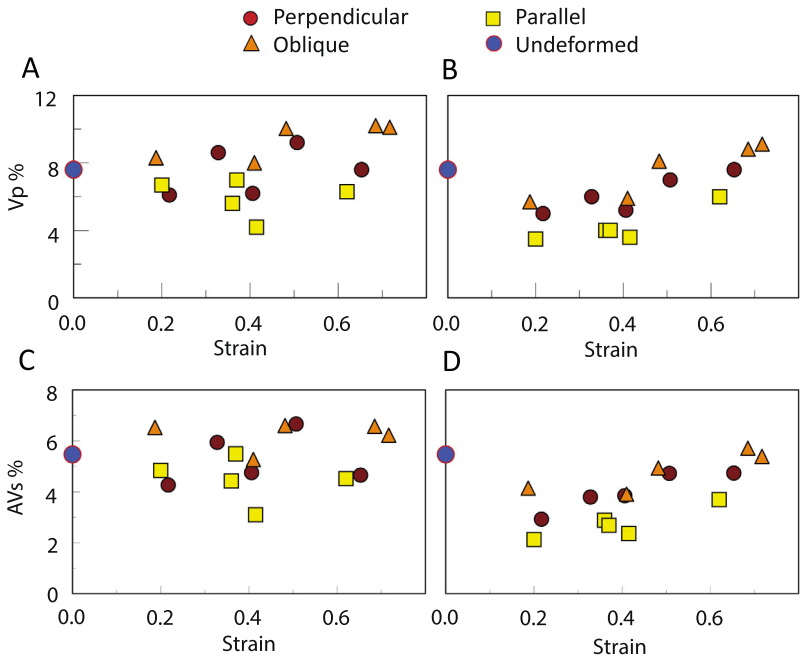

Fig. 6. Anisotropy of seismic wave velocities *Vp* and *Vs* in %, calculated by weighted area for samples in three different configurations. Samples deformed in perpendicular, oblique, and parallel geometries are shown by red circles, orange triangles and yellow squares, respectively. Blue circles show the anisotropic properties of the starting material. (A) and (C) show the seismic wave velocities *Vp* and *AVs*, respectively, calculated using all the data, which includes a small number of relict grains. (B) and (D) show the calculated seismic velocities using grains with diameter smaller than 50 μm representing only the recrystallized grains (neoblasts). Within the set of neoblasts, anisotropy increases with strain for all three samples configurations. Neither *Vp* nor *AVs* anisotropy reaches a plateau indicating that steady state was not achieved. (For interpretation of the references to color in this figure legend, the reader is referred to the web version of this article.)

a steady-state texture, but instead represents a transient stage in the evolution towards axially symmetric texture. Due to the limited maximum strain of a triaxial deformation experiment, it is unclear how much additional strain would be required to fully obscure the pre-existing texture.

4.4. Seismic anisotropy

The results of this study emphasize the important role of deformation history on texture evolution, and highlight the impact of transient CPO on the interpretation of seismic anisotropy (Skemer et al., 2012). Fig. 5 shows the predicted anisotropic signature of the undeformed sample and samples with the highest strains from experiments in the perpendicular, oblique and parallel configurations. EBSD data used in this calculation are weighted by grain area, so a few larger relict grains can have a proportionately large influence on the results. It is clear that the samples deformed in each configuration exhibit distinct seismic properties, both in terms of the magnitude and orientation of the anisotropy. As with the CPO, seismic anisotropy did not achieve steady-state in our experiments, but rather continued to evolve throughout the full range of strains achieved here (Fig. 6). The long transient stage of texture evolution could readily generate shear wave splitting signatures that do not represent the present day mantle flow direction. Similarly, the transient reorganization of CPO could produce an apparently weak CPO that would manifest itself as weak anisotropy.

Mantle flow around subduction-zones, as an example, is complicated by large temperature and compositional gradients, horizontal and sub-vertical flow in the direction of convergence, and trench parallel flow, particularly near slab edges (Blackman and Kendall, 2002; Faccenda and Capitanio, 2012; Jadamec and Billen, 2012; McKenzie, 1979). The complexity of this environment has presented a challenge to the interpretation of seismic anisotropy (Long and Becker, 2010). Many of the features of plate boundary seismic anisotropy have been attributed to the effects of pressure (Jung et al., 2009), water content (Katayama and Karato, 2006; Long and Becker, 2010), asthenospheric entrainment by the subducted slab (Song and Kawakatsu, 2012), or 3-D flow patterns (Faccenda and Capitanio, 2012; Long and Silver, 2008). Based on our experimental results, other observations from naturally deformed rocks (Michibayashi and Mainprice, 2004; Skemer et al., 2012; Warren et al., 2008; Webber et al., 2010), and data from numerical simulations (Castelnau et al., 2009; Di Leo et al., 2014) it is increasingly evident that deformation history must also be a factor in the interpretation of seismic anisotropy.

5. Conclusions

Experiments performed on natural Åheim dunite with pre-existing texture were deformed to strains up to 0.7. Using three different pre-existing texture orientations we show that deformation history of olivine aggregates greatly influence the way texture evolves with strain. Based on quantification of pole figures in terms of texture strength, symmetry, and alignment, we assert that the texture in all three experimental configurations did not reach a steady state. Rapid changes in mantle flow direction may be associated with long transient stages in which texture evolves slowly towards a steady state. It is concluded that any interpretation of seismic anisotropy in terms of mantle flow must consider the integrated deformation history of the region of interest.

Acknowledgements

The authors thank Brandon Mahan, John Keefner, and Gyorgy Falus for helpful discussions. Ian Jackson kindly provided the block of Åheim dunite used in these experiments. Shun Karato and Zhenting Jiang are gratefully acknowledged for enabling and assisting with the FTIR measurements. Reviewers are thanked for their constructive input. The research is supported by NSF EAR-1141795 (to PS).

References

Abramson, E.H., Brown, M., Slutsky, L.J., Zaug, J., 1997. The elastic constants of San Carlos olivine up to 17 GPa. J. Geophys. Res. 102, 12,252–212,263.

Becker, T.W., Kellogg, J.B., Ekström, G., O'Connell, R.J., 2003. Comparison of azimuthal seismic anisotropy from surface waves and finite strain from global mantle-circulation models. Geophys. J. Int. 155, 696–714. http://dx.doi.org/10.1046/j.1365-246X.2003.02085.x.

Becker, T.W., Schulte-Pelkum, V., Blackman, D.K., Kellogg, J.B., O'Connell, R.J., 2006. Mantle flow under the western United States from shear wave splitting. Earth Planet. Sci. Lett. 247, 235–251. http://dx.doi.org/10.1016/j.epsl.2006.05.010.

Bell, D.R., Rossman, G.R., Maldener, J., Endisch, D., Rauch, F., 2003. Hydroxide in olivine: a quantitative determination of the absolute amount and calibration of the IR spectrum. J. Geophys. Res. Solid Earth (1978–2012) 108. http://dx.doi.org/10.1029/2001JB000679.

Ben Ismaïl, W., Mainprice, D., 1998. An olivine fabric database: an overview of upper mantle fabrics and seismic anisotropy. Tectonophysics 296, 145–157. http://dx.doi.org/10.1016/S0040-1951(98)00141-3.

Berckhemer, H., Kampfmann, W., Aulbach, E., Schmeling, H., 1982. Shear modulus and Q of forsterite and dunite near partial melting from forced-oscillation experiments. Phys. Earth Planet. Inter. 29, 30–41.

Blackman, D.K., Kendall, J., 2002. Seismic anisotropy in the upper mantle 2. Predictions for current plate boundary flow models. Geochem. Geophys. Geosyst. 3. http://dx.doi.org/10.1029/2001GC000247.

Bystricky, M., Kunze, K., Burlini, L., Burg, J.-P., 2000. High shear strain of olivine aggregates: rheological and seismic consequences. Science 290, 1564–1567. http://dx.doi.org/10.1126/science.290.5496.1564.

Castelnau, O., Blackman, D., Becker, T., 2009. Numerical simulations of texture development and associated rheological anisotropy in regions of complex mantle flow. Geophys. Res. Lett. 36, L12304. http://dx.doi.org/10.1029/2009GL038027.

Chopra, P.N., Paterson, M.S., 1981. The experimental deformation of dunite. Tectonophysics 78, 453–473.

Chopra, P.N., Paterson, M.S., 1984. The role of water in the deformation of dunite. J. Geophys. Res., Solid Earth 89, 7861–7876.

Conrad, C.P., Behn, M.D., Silver, P.G., 2007. Global mantle flow and the development of seismic anisotropy: differences between the oceanic and continental upper mantle. J. Geophys. Res. 112, B07317. http://dx.doi.org/10.1029/2006JB004608.

Couvy, H., Frost, D.J., Heidelbach, F., Nyilas, K., Ungár, T., Mackwell, S.J., Cordier, P., 2004. Shear deformation experiments of forsterite at 11 GPa–1400 °C in the multianvil apparatus. Eur. J. Mineral. 16, 877–889. http://dx.doi.org/10.1127/0935-1221/2004/0016-0877.

Di Leo, J.F., Walker, A.M., Li, Z.H., Wookey, J., Ribe, N.M., Kendall, J.M., Tommasi, A., 2014. Development of texture and seismic anisotropy during the onset of subduction. Geochem. Geophys. Geosyst. 15, 192–212. http://dx.doi.org/10.1002/2013GC005032.

Druiventak, A., Trepmann, C.A., Renner, J., Hanke, K., 2011. Low-temperature plasticity of olivine during high stress deformation of peridotite at lithospheric conditions—an experimental study. Earth Planet. Sci. Lett. 311, 199–211. http://dx.doi.org/10.1016/j.epsl.2011.09.022.

Faccenda, M., Capitanio, F., 2012. Development of mantle seismic anisotropy during subduction-induced 3-D flow. Geophys. Res. Lett. 39. http://dx.doi.org/10.1029/2012GL051988.

Flievoet, T.F., Drury, M.R., Chopra, P.N., 1999. Crystallographic preferred orientations and misorientations in some olivine rocks deformed by diffusion or dislocation creep. Tectonophysics 303, 1–27. http://dx.doi.org/10.1016/S0040-1951(98)00250-9.

Hansen, L.N., Zhao, Y.-H., Zimmerman, M.E., Kohlstedt, D.L., 2014. Protracted fabric evolution in olivine: implications for the relationship among strain, crystallographic fabric, and seismic anisotropy. Earth Planet. Sci. Lett. 387, 157–168. http://dx.doi.org/10.1016/j.epsl.2013.11.009.

Hansen, L.N., Zimmerman, M.E., Kohlstedt, D.L., 2012. Laboratory measurements of the viscous anisotropy of olivine aggregates. Nature 492, 415–418. http://dx.doi.org/10.1038/nature11671.

Hirth, G., Kohlstedt, D., 2003. Rheology of the upper mantle and the mantle wedge: a view from the experimentalists. Geophys. Monogr. 138, 83–105. http://dx.doi.org/10.1029/138GM06.

Jackson, I., Paterson, M., Fitz Gerald, J., 1992. Seismic wave dispersion and attenuation in Åheim dunite: an experimental study. Geophys. J. Int. 108, 517–534.

Jadamec, M., Billen, M., 2012. The role of rheology and slab shape on rapid mantle flow: three-dimensional numerical models of the Alaska slab edge. J. Geophys. Res. B, Solid Earth Planets (1978–2012), 117. http://dx.doi.org/10.1029/2011JB008563.

Jin, Z., Bai, Q., Kohlstedt, D., 1994. High-temperature creep of olivine crystals from four localities. Phys. Earth Planet. Inter. 82, 55–64.

Jung, H., Karato, S.-i., 2001. Water-induced fabric transitions in olivine. Science 293, 1460–1463. http://dx.doi.org/10.1126/science.1062235.

Jung, H., Katayama, I., Jiang, Z., Hiraga, T., Karato, S., 2006. Effect of water and stress on the lattice-preferred orientation of olivine. Tectonophysics 421, 1–22. http://dx.doi.org/10.1016/j.tecto.2006.02.011.

Jung, H., Mo, W., Green, H.W., 2009. Upper mantle seismic anisotropy resulting from pressure-induced slip transition in olivine. Nat. Geosci. 2, 73–77. http://dx.doi.org/10.1038/ngeo389.

Kaminski, E., Ribe, N.M., 2001. A kinematic model for recrystallisation and texture development in olivine polycrystals. Earth Planet. Sci. Lett. 189, 257–267. http://dx.doi.org/10.1016/S0012-821X(01)00356-9.

Kaminski, E., Ribe, N.M., Browaeys, J.T., 2004. D-Rex, a program for calculation of seismic anisotropy due to crystal lattice preferred orientation in the convective upper mantle. Geophys. J. Int. 158, 744–752. http://dx.doi.org/10.1111/j.1365-246X.2004.02308.x.

Karato, S.-i., 1988. The role of recrystallization in the preferred orientation of olivine. Phys. Earth Planet. Inter. 51, 107–122.

Karato, S.-i., Jung, H., Katayama, I., Skemer, P., 2008. Geodynamic significance of seismic anisotropy of the upper mantle: new insights from laboratory studies. Annu. Rev. Earth Planet. Sci. 36, 59–95. http://dx.doi.org/10.1146/annurev.earth.36.031207.124120.

Karato, S.-i., Wu, P., 1993. Rheology of the upper mantle: a synthesis. Science, 771–778.

Katayama, I., Karato, S.-i., 2006. Effect of temperature on the B- to C-type olivine fabric transition and implication for flow pattern in subduction zones. Phys. Earth Planet. Inter. 157, 33–45. http://dx.doi.org/10.1016/j.pepi.2006.03.005.

Keefner, J., Mackwell, S., Kohlstedt, D., Heidelbach, F., 2011. Dependence of dislocation creep of dunite on oxygen fugacity: implications for viscosity variations in Earth's mantle. J. Geophys. Res. Solid Earth 116, 1915. http://dx.doi.org/10.1029/2010JB007748.

Li, Z.H., Di Leo, J.F., Ribe, N.M., 2014. Subduction-induced mantle flow, finite strain and seismic anisotropy: numerical modeling. J. Geophys. Res. B, Solid Earth Planets.

Long, M.D., Becker, T.W., 2010. Mantle dynamics and seismic anisotropy. Earth Planet. Sci. Lett. 297, 341–354. http://dx.doi.org/10.1002/2014JB010996.

Long, M.D., Silver, P.G., 2008. The subduction zone flow field from seismic anisotropy: a global view. Science 319, 315–318. http://dx.doi.org/10.1126/science.1150809.

Long, M.D., Silver, P.G., 2009. Mantle flow in subduction systems: the subslab flow field and implications for mantle dynamics. J. Geophys. Res. Solid Earth (1978–2012) 114. http://dx.doi.org/10.1029/2008JB006200.

Mackwell, S.J., Kohlstedt, D.L., 1990. Diffusion of hydrogen in olivine: implications for water in the mantle. J. Geophys. Res. Solid Earth (1978–2012) 95, 5079–5088.

Mainprice, D., 1990. A Fortran program to calculate seismic anisotropy from the lattice preferred orientation of minerals. Comput. Geosci. 16, 385–393.

Mainprice, D., 2007. Seismic anisotropy of the deep Earth from a mineral and rock physics perspective. In: Treatese of Geophysics, vol. 2, pp. 437–491. http://dx.doi.org/10.1016/B978-044452748-6.00045-6.

Mainprice, D., Barruol, G., Ben Ismaïl, W., 2000. The seismic anisotropy of the Earth's Mantle: from single crystal to polycrystal. In: Karato, S.-i., Forte, A.M., Liebermann, R.C., Master, G., Stixrude, L. (Eds.), Earth's Deep Interior: Mineral Physics and Tomography from the Atomic to the Global Scale. American Geophysical Union, Washington, DC, pp. 237–264. http://dx.doi.org/10.1029/GM117p0237.

McKenzie, D., 1979. Finite deformation during fluid flow. Geophys. J. R. Astron. Soc. 58, 689–715.

Mendelson, M.I., 1969. Average grain size in polycrystalline ceramics. J. Am. Ceram. Soc. 52, 443–446.

Michibayashi, K., Mainprice, D., 2004. The role of pre-existing mechanical anisotropy on shear zone development within oceanic mantle lithosphere: an example from the Oman ophiolite. J. Petrol. 45, 405–414. http://dx.doi.org/10.1093/petrology/egg099.

Montagner, J.-P., 2002. Upper mantle low anisotropy channels below the Pacific Plate. Earth Planet. Sci. Lett. 202, 263–274. http://dx.doi.org/10.1016/S0012-821X(02)00791-4.

Montagner, J.-P., Tanimoto, T., 1991. Global upper mantle tomography of seismic velocities and anisotropies. J. Geophys. Res. 96, 20337–20351.

Montési, L.G., 2013. Fabric development as the key for forming ductile shear zones and enabling plate tectonics. J. Struct. Geol. 50, 254–266. http://dx.doi.org/10.1016/j.jsg.2012.12.011.

Nicolas, A., Boudier, F., Boullier, A.M., 1973. Mechanism of flow in naturally and experimentally deformed peridotites. Am. J. Sci. 273, 853–876.

Nicolas, A., Christensen, N.I., 1987. Formation of anisotropy in upper mantle peridotites: a review. Geodyn. Ser. 16, 111–123.

Nitsan, U., 1974. Stability field of olivine with respect to oxidation and reduction. J. Geophys. Res. 79, 706–711.

Paterson, M.S., 1982. The determination of hydroxyl by infrared absorption in quartz, silicates glasses and similar materials. Bull. Miner. 105, 20–29.

Ramsay, J., 1967. Folding and Fracturing of Rock. MacGraw–Hill, New York.

Raterron, P., Chen, J., Li, L., Weidner, D., Cordier, P., 2007. Pressure-induced slip-system transition in forsterite: single-crystal rheological properties at mantle pressure and temperature. Am. Mineral. 92, 1436–1445. http://dx.doi.org/10.2138/am.2007.2474.

Ribe, N.M., Yu, Y., 1991. A theory for plastic deformation and textural evolution of olivine polycrystals. J. Geophys. Res. Solid Earth (1978–2012) 96, 8325–8335.

Savage, M., 1999. Seismic anisotropy and mantle deformation: what have we learned from shear wave splitting? Rev. Geophys. 37, 65–106.

Silver, P., Mainprice, D., Ismail, W.B., Tommasi, A., Barruol, G., 1999. Mantle structural geology from seismic anisotropy. In: Fei, Y., Bertka, C., Mysen, B.O. (Eds.), Mantle Petrology: Field Observations and High Pressure Experimentation. A Tribute to Francis R. (Joe) Boyd. The Geochemical Society, Houston.

Skemer, P., Katayama, I., Jiang, Z., Karato, S.-i., 2005. The misorientation index: development of a new method for calculating the strength of lattice-preferred orientation. Tectonophysics 411, 157–167. http://dx.doi.org/10.1016/j.tecto.2005.08.023.

Skemer, P., Sundberg, M., Hirth, G., Cooper, R., 2011. Torsion experiments on coarse-grained dunite: implications for microstructural evolution when diffusion creep is suppressed. Geol. Soc. (Lond.) Spec. Publ. 360, 211–223. http://dx.doi.org/10.1144/sp360.12.

Skemer, P., Warren, J.M., Hansen, L.N., Hirth, G., Kelemen, P.B., 2013. The influence of water and LPO on the initiation and evolution of mantle shear zones. Earth Planet. Sci. Lett. 375, 222–233. http://dx.doi.org/10.1016/j.epsl.2013.05.034.

Skemer, P., Warren, J.M., Hirth, G., 2012. The influence of deformation history on the interpretation of seismic anisotropy. Geochem. Geophys. Geosyst. 13. http://dx.doi.org/10.1029/2011GC003988.

Skemer, P., Warren, J.M., Kelemen, P.B., 2010. Microstructural and rheological evolution of a mantle shear zone. J. Petrol. 51, 43–53. http://dx.doi.org/10.1093/petrology/egp057.

Song, T.R.A., Kawakatsu, H., 2012. Subduction of oceanic asthenosphere: evidence from sub-slab seismic anisotropy. Geophys. Res. Lett. 39. http://dx.doi.org/10.1029/2012GL052639.

Tanimoto, T., Anderson, D.L., 1985. Lateral heterogeneity and azimuthal anisotropy of the upper mantle: Love and Rayleigh waves 100–250 s. J. Geophys. Res. Solid Earth (1978–2012) 90, 1842–1858.

Tommasi, A., Knoll, M., Vauchez, A., Signorelli, J.W., Thoraval, C., Logé, R., 2009. Structural reactivation in plate tectonics controlled by olivine crystal anisotropy. Nat. Geosci. 2, 423–427. http://dx.doi.org/10.1038/ngeo528.

Tommasi, A., Mainprice, D., Canova, G., Chastel, Y., 2000. Viscoplastic self-consistent and equilibrium-based modeling of olivine lattice preferred orientations: implications for upper mantle seismic anisotropy. J. Geophys. Res. 105, 7893–7908.

Van der Wal, D., Chopra, P., Drury, M., Gerald, J.F., 1993. Relationships between dynamically recrystallized grain size and deformation conditions in experimentally deformed olivine rocks. Geophys. Res. Lett. 20, 1479–1482.

Vollmer, F.W., 1990. An application of eigenvalue methods to structural domain analysis. Geol. Soc. Am. Bull. 102, 786–791.

Warren, J.M., Hirth, G., Kelemen, P.B., 2008. Evolution of olivine lattice preferred orientation during simple shear in the mantle. Earth Planet. Sci. Lett. 272, 501–512. http://dx.doi.org/10.1016/j.epsl.2008.03.063.

Webber, C., Newman, J., Holyoke III, C.W., Little, T., Tikoff, B., 2010. Fabric development in cm-scale shear zones in ultramafic rocks, Red Hills, New Zealand. Tectonophysics 489, 55–75. http://dx.doi.org/10.1016/j.tecto.2010.04.001.

Wendt, A.S., Mainprice, D., Rutter, E., Wirth, R., 1998. A joint study of experimental deformation and experimentally induced microstructures of pretextured peridotites. J. Geophys. Res. 103, 18205–18221.

Wenk, H.R., Bennett, K., Canova, G.R., Molinari, A., 1991. Modelling plastic deformation of peridotite with the self-consistent theory. J. Geophys. Res. 96, 8337–8349.

Wenk, H.R., Christie, J.M., 1991. Review paper. Comments on the interpretation of deformation textures in rocks. J. Struct. Geol. 13, 1091–1110.

Wenk, H.R., Tomé, C.N., 1999. Modeling dynamic recrystallisation of olivine aggregates deformed in simple shear. J. Geophys. Res., Solid Earth 104, 25513–25527.

Zhang, S., Karato, S.-i., 1995. Lattice preferred orientation of olivine aggregates deformed in simple shear. Nature 375, 774–777. http://dx.doi.org/10.1038/375774a0.